actuators

MDPI

Article

Structural Design and Kinematic Analysis of Cable-Driven Soft Robot

Feng Wei, Kun Luo, Yeming Zhang * and Jianfeng Jiang

School of Mechanical and Power Engineering, Henan Polytechnic University, Jiaozuo 454003, China; elite@hpu.edu.cn (F.W.); luokun9816@163.com (K.L.); yianti_an@126.com (J.J.)
* Correspondence: zym@hpu.edu.cn

Abstract: Continuous robots have attracted more and more attention from the robotics community due to their high degree of flexibility and pliability, and have shown great potential for application in a variety of fields. With the continuous progress of material science, control technology, and artificial intelligence, the performance and application range of soft robotics have been further expanded, in which the cable drive has the advantages of large workspace, high flexibility, etc. The cable-driven soft robotic arm serves as an ultra-redundant robot that can operate in cramped and confined environments. In this paper, a cable-driven soft robot based on soft continuums and a cross gimbal is presented. The kinematics of the cable-driven soft robot is modeled and the mapping relations of the kinematics are solved by the D–H method and piecewise constant curvature, and the relations between the cable length, joint angle, and pose are further derived. Finally, the motion space of the cable-driven soft robot in the three-dimensional coordinate system is obtained by MATLAB2021b, and the single-segment soft body is simulated and analyzed using ADAMS to compare the theoretical data with the actual data and verify the reliability of this structure and method.

Keywords: cable-driven; continuum robotic arm; piecewise constant curvature; D–H method; kinematics; simulation

check for updates

Citation: Wei, F.; Luo, K.; Zhang, Y.; Jiang, J. Structural Design and Kinematic Analysis of Cable-Driven Soft Robot. *Actuators* **2024**, *13*, 497. https://doi.org/10.3390/act13120497

Academic Editor: Hamed Rahimi Nohooji

Received: 19 September 2024
Revised: 27 November 2024
Accepted: 3 December 2024
Published: 4 December 2024

Copyright: © 2024 by the authors. Licensee MDPI, Basel, Switzerland. This article is an open access article distributed under the terms and conditions of the Creative Commons Attribution (CC BY) license (https://creativecommons.org/licenses/by/4.0/).

1. Introduction

Compared with the traditional rigid robotic arm, soft robotics has a higher degree of flexibility, adaptability, dexterity, and a wider range of application areas, mostly suitable for small spaces and complex paths, especially in military, aerospace, and medical equipment contexts, where it is the most widely used. Soft robotics can be divided into two types: in the first, the connecting rod of the mechanical arm is made of elastic material, and the connecting rod, that is, the distributed soft mechanical arm, is soft; in the second, the connecting rod of the robot is rigid, soft, and only exists in the joint, which is called a soft joint robot arm because the stiffness of its joints can be changed, so that it can be called a variable stiffness joint. In 1967, Webster designed what is recognized as the earliest cable-driven soft robot, setting a precedent for the use of a cable to drive the movement of robotic arm joints and providing a new direction for the subsequent design of robotic arm structures [1]. Li designed a cable-driven continuum robot with a soft skeleton having multiple bendable continuums, in which multiple disks are mounted on each segment of the soft skeleton [2]. Walker's team developed a number of snake-like robotic arms, including pneumatic artificial muscles and cable drives [3,4]. Pang proposed a seven-degree-of-freedom cable-driven robotic arm with a tensioning mechanism that can be tightened in real time as the arm moves to prevent the cable from slackening [5]. Renda designed a soft manipulator that mimics the tentacles of an octopus, where the body of the manipulator consists of a conical silica gel and is driven by several cables immersed in the silica gel body, where the driving cables are fixed at different distances from the base by means of rigid plastic disks inside the manipulator arm [6]. Cao proposed a novel tendon-driven continuum robot with two modules and a soft skeleton consisting of coil springs, each of which is redundantly driven

by four parallel tendons, which in turn ensures the soft motion of the robot [7]. Runciman designed a medical robot for the treatment of gastric cancer that folds around the endoscope, unfolds when it reaches the work area, and transmits force through the surrounding cables [8]. Qi designed a cable-driven soft robot for use in minimally invasive surgery based on the segmental constant curvature method, and proposed a navigation method for semi-autonomous interventional procedures based on vascular constraints, which was validated by simulations in glass vessels [9]. McMahan designed an elephant trunk-like pneumatic OctArm robot, controlled by inflating and deflating a chamber inside the robot, and experimented with the robot in different environments [10]. Calisti controlled the motion of an octopus-like robot by embedding cables in silicone to enable the robot to perform tasks in different situations [11]. Deimel designed a humanoid mechanical gripper called THE RBO Hand 2, which assesses whether the material on the top and bottom of the finger is deformable or not to control the finger bending. This robot controls the movement of the mechanical gripper by changing the magnitude of air pressure [12]. Gu designed a cable-driven serpentine manipulator and derived a motion path and an iterative inverse kinematic algorithm for RDSM in a multi-obstacle environment using segmented Bessel curves [13]. Zhang designed a soft robotic arm driven by a rotatable cable and performed a dynamic analysis of the arm taking into account the friction between the cable and the pipe [14]. Lihas designed TSM, a soft robot arm that combines the cable with a Bowden tube. This robot arm combines the pneumatic bellows with the cable. TSM has better resistance to axial stretching, tangential bending, and torsion, which greatly enhances the balance between rigidity and flexibility [15]. Khalil proposed a physics-based design optimization method for cable-driven soft robotic manipulators, aimed at enhancing bending performance through structural design improvements. Four key design criteria were considered: cross-sectional shape, material, gap shape, and gap size. Finite element modeling was used to analyze their impact on displacement and bending angle, with material variation having the greatest effect on performance, followed by gap shape and gap size [16]. Cieślak proposed the design and analysis of an elephant trunk-like soft manipulator that can be used for the transportation of bulk and liquid materials. This manipulator is composed of rigid inserts and elastic elements (helical springs) connected in series, allowing it to bend and move in a soft manner [17]. Wang proposed a soft robotic surgical system inspired by octopus tentacles, made from soft materials that can adapt to the complex environments of the thoracic and pericardial cavities. The system is cable-driven and remotely operated by a surgeon, offering high flexibility and control, enabling it to perform minimally invasive surgical procedures. Experiments on pigs validated the system's capability to enter the thoracic and pericardial cavities and carry out various surgical tasks such as biopsy, ligation, and ablation without causing damage to the surrounding tissues [18]. Zarebidoki proposed the design, modeling, and development of a cable-driven underwater manipulator (UM) and a four-finger adaptive, tendon-driven robotic gripper, primarily for the delicate manipulation of marine biological samples. The active force control of the tendon-driven gripper ensures gentle and precise grasping, manipulation, and transportation of marine samples without damaging their tissues [19]. Zhou proposed a novel cable-driven single backbone continuum robot inspired by fish bones. The central backbone is composed of multiple bio-inspired fish bone units arranged in a cross pattern, which provides excellent one-dimensional bending capability and reduced motion coupling. The unique structure of the central backbone simplifies the theoretical model, enhancing the modeling accuracy and controllability of the robot [20]. Inspired by the elephant's trunk, Zhang developed a modular tensile structure with programmable stiffness for cable-driven continuum robots. The author created a mechanical model to predict the robot's configuration under different stiffness distributions and fabricated a 12-module continuum robot, demonstrating its deformation patterns. By adjusting the distribution of spring stiffness, the robot can navigate through passages of varying curvatures, showcasing its potential in applications requiring adaptive curvature and conformal interaction [21]. Zhang proposed a novel design for a cable-driven continuum robot capable of multiple modes of movement, including bending

and contraction. This robot is composed of a tensile structure made up of transverse rods, longitudinal rods, springs, and cables. A mechanical model was established using position-based finite element methods to analyze the kinematics of the robot under different modes of movement. Based on the theoretical results, a three-segment continuum robot prototype was fabricated, demonstrating a 90-degree bending angle and a 40% contraction ratio.

However, in practice, the cable-driven soft robotic arm must take into account the possible interference between the cable and the elastic skeleton, so its actual movement space will have a large gap with the theoretical value. In summary, in order to meet the dexterity requirements and operational needs of cable-driven soft robotics, a cable-driven soft robotic arm based on soft continuums and cross gimbals is designed to expand the movement space of cable-driven soft robotics, which is capable of full-dimensional and large-angle movements. This paper is divided into two parts. Firstly, the structure of a suitable cable-driven soft manipulator is designed. Secondly, the motion model of the robot arm is established, the motion mapping is solved, the motion space of the robot arm is identified, and the motion performance and reliability of the robot arm are verified by simulation.

2. Structural Design and Kinematic Modeling of Robotic Arms

2.1. Structural Design

The structure of the cable-driven soft robotic arm is shown in Figure 1. The robotic arm mainly consists of three soft continuums, two cross gimbals, and six baffles, and each soft body and cross gimbal is driven by three cables, which are spaced 120° apart on the cloth cable disks. The driving cables are steel wire cables with diameter d_1. The soft body is made of a nickel–titanium alloy spring with length l. The radius from the center of the through hole to the center of the cloth cable disk is r.

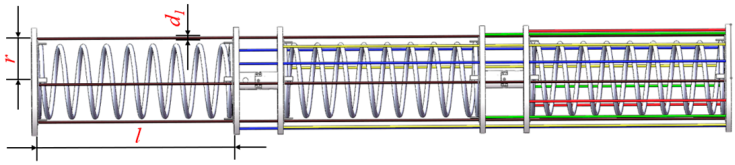


Figure 1. Structure of the cable-driven soft robot arm.

The kinematic mapping is solved by the piecewise constant curvature method and the D–H method. The mapping relationship between the three spaces of actuator space, configuration space, and task space is shown in Figure 2. The variable in the actuator space is the cable length $l_i(i = 1, 2 \cdots 15)$. The variable in the configuration space is $\varphi_1, \theta_1, \varphi_2, \theta_2, \varphi_3, \theta_3, \alpha_1, \beta_1, \alpha_2, \beta_2$. Where φ_i is the angle of rotation of the soft joint, θ_i is the angle of bending, α_i is the angle of rotation of the gimbal, and β_i is the angle of bending, and the variable in the operating space is the end pose (x, y, z) of the robotic arm in the Cartesian coordinate system.

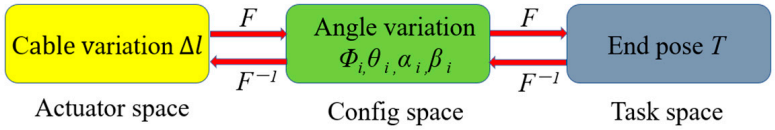


Figure 2. Kinematic mapping relationship.

2.2. Kinematic Modeling of a Single-Segmented Soft Body

The following three assumptions are made:

Assumption 1. *The central curve of the spring is always in one plane.*

Assumption 2. *The segment curvature of the spring is constant.*

Assumption 3. *When the arm is in a straight line state, the X-axis of all coordinate systems points to cable hole 1.*

2.2.1. Soft Body Modeling

The model of a single-segment soft body is shown in Figure 3, where the coordinate origin of coordinate system $O_1 - X_1Y_1Z_1$ is located on the bottom surface of the soft body, the coordinate origin of coordinate system $O_2 - X_2Y_2Z_2$ is located on the top surface of the soft body, and R_a is the bending radius of the soft body.

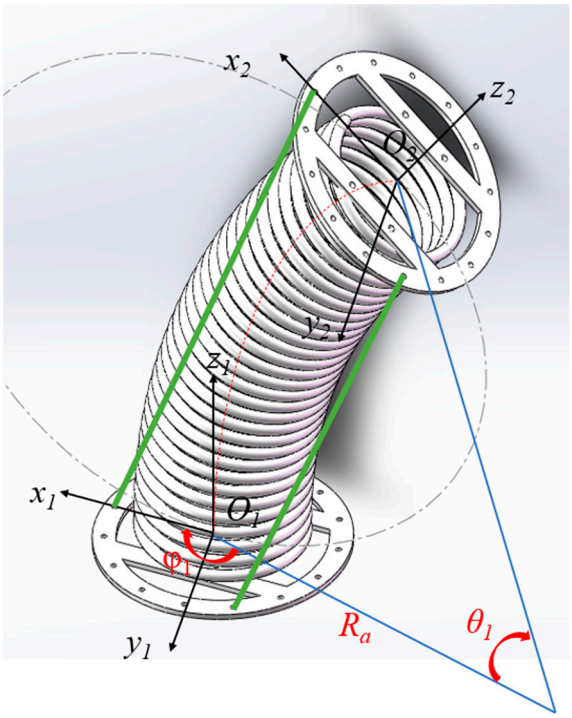


Figure 3. Soft body model.

2.2.2. Mapping the Configuration Space to the Task Space

Forward kinematic analysis.

From coordinate system $O_1 - X_1Y_1Z_1$ to coordinate system $O_2 - X_2Y_2Z_2$ can be viewed as coordinate system $O_1 - X_1Y_1Z_1$ rotated φ_1 around the z axis, then rotated θ_1 around the y axis, then translated $\frac{2}{\rho}\sin(\frac{\theta_1}{2})$ along the z axis, and finally rotated φ_1 around the z axis to obtain coordinate system $O_2 - X_2Y_2Z_2$, the transformation matrix between coordinate systems can be expressed as:

$$
\begin{aligned}
{}^1_2T &= R_1 \cdot R_2 \cdot T_1 \cdot R_3 \\
&= \begin{bmatrix} C\theta_1C^2\varphi_1 + S^2\varphi_1 & -C\varphi_1S\varphi_1V\theta_1 & C\varphi_1S\theta_1 & \frac{C\varphi_1V\theta_1}{\rho} \\ -C\varphi_1S\varphi_1V\theta_1 & C^2\varphi_1 + C\theta_1S^2\varphi_1 & S\varphi_1S\theta_1 & \frac{S\varphi_1V\theta_1}{\rho} \\ -C\varphi_1S\theta_1 & -S\varphi_1S\theta_1 & C\theta_1 & \frac{S\theta_1}{\rho} \\ 0 & 0 & 0 & 1 \end{bmatrix}
\end{aligned} \tag{1}
$$

where $C\theta_1 = Cos\theta_1, V\theta_1 = 1 - Cos\theta_1, S\theta_1 = Sin\theta_1, C\varphi_1 = Cos\varphi_1, S\varphi_1 = Sin\varphi_1, \rho = \frac{\theta_1}{l}$. ρ is the curvature of the central axis of the spring.

Inverse kinematic analysis:

$$ {}^{1}_{2}T = \begin{pmatrix} {}^{1}_{2}R & {}^{1}_{2}P \\ 0 & 1 \end{pmatrix} = \begin{pmatrix} n & o & a & P \\ 0 & 0 & 0 & 1 \end{pmatrix} = \begin{pmatrix} n_x & o_x & a_x & p_x \\ n_y & o_y & a_y & p_y \\ n_z & o_z & a_z & p_z \\ 0 & 0 & 0 & 1 \end{pmatrix} \tag{2} $$

From Equations (1) and (2):

$$ p_x = \frac{\cos\varphi_1(1-\cos\theta_1)}{\rho} \tag{3} $$

$$ p_y = \frac{\sin\varphi_1(1-\cos\theta_1)}{\rho} \tag{4} $$

$$ p_z = \frac{\sin\theta_1}{\rho} \tag{5} $$

From Equations (3) and (4):

$$ \varphi_1 = \arctan\left(\frac{p_y}{p_x}\right) \tag{6} $$

$$ \theta_1 = 2\arctan\frac{p_y}{p_z\sin\varphi_1} \tag{7} $$

2.2.3. Mapping Actuator Space to the Configuration Space

In order to obtain the forward kinematics from the actuator space to the configuration space more conveniently, the inverse kinematics from the actuator space to the configuration space is derived here first.

Inverse kinematic analysis.

Inverse kinematics can solve the length of the rope when the end pose is known. First, the rotation angle and bending angle are obtained through the end pose, and then the length of the rope is obtained, so that the ideal pose can be achieved by controlling the cable. A schematic diagram of the bending of a single segment of the soft body is shown in Figure 4. R_{11}, R_{12}, R_{13}, are the bending radii of cables 1, 2, and 3 in the ith segment of the soft body, respectively.

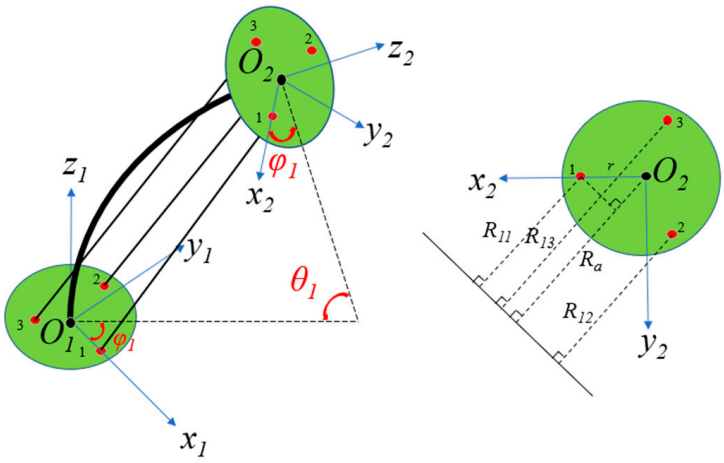


Figure 4. Schematic diagram of bending.

The lengths of R_{11}, R_{12}, R_{13} can be calculated from Figure 4:

$$R_{11} = R_a - r\cos\varphi_1 \tag{8}$$

$$R_{12} = R_a - r\cdot\cos(\frac{2\pi}{3} - \varphi_1) \tag{9}$$

$$R_{13} = R_a - r\cdot\cos(\frac{4\pi}{3} - \alpha_1) \tag{10}$$

From Equations (8)–(10):

$$l_{1,1} = 2\sin\frac{\theta_1}{2}(\frac{l}{\theta_1} - r\cos\varphi_1) \tag{11}$$

$$l_{1,2} = 2\sin\frac{\theta_1}{2}(\frac{l}{\theta_1} - r\cos(\frac{2\pi}{3} - \varphi_1)) \tag{12}$$

$$l_{1,3} = 2\sin\frac{\theta_1}{2}(\frac{l}{\theta_1} - r\cos(\frac{4\pi}{3} - \varphi_1)) \tag{13}$$

where $l_{1,1}, l_{1,2}, l_{1,3}$ are the respective lengths of cables 1, 2, and 3 on the first soft body, r is the distance between the coordinate origin o and the cable hole.

Forward kinematic analysis.

From Equations (11)–(13):

$$2l_{1,1} - l_{1,2} - l_{1,3} = -6\sin\frac{\theta_1}{2}\cos\varphi_1$$

$$l_{1,2} - l_{1,3} = -2\sqrt{3}\sin\frac{\theta_1}{2}\sin\varphi_1$$

$$\frac{\sqrt{3}(l_{1,2} - l_{1,3})}{2l_{1,1} - l_{1,2} - l_{1,3}} = \tan\varphi_1$$

$$\varphi_1 = \arctan\frac{\sqrt{3}(l_{1,2} - l_{1,3})}{2l_{1,1} - l_{1,2} - l_{1,3}} \tag{14}$$

From Equations (11) and (13):

$$l_{1,3} - l_{1,1} = r\sin\frac{\theta_1}{2}(3\cos\varphi_1 + \sqrt{3}\sin\varphi_1)$$

$$\sin\frac{\theta_1}{2} = \frac{l_{1,3} - l_{1,1}}{r\left(3\cos\varphi_1 + \sqrt{3}\sin\varphi_1\right)}$$

$$\theta_1 = 2arcsin\frac{l_{1,3} - l_{1,1}}{r\left(3\cos\varphi_1 + \sqrt{3}\sin\varphi_1\right)} \tag{15}$$

2.3. Kinematic Modeling of Mobile Joints

2.3.1. Cross Universal Joint Model

The model of the cross gimbal is shown in Figure 5 and the structural drawing is shown in Figure 6, where d is the distance between the center of the cross gimbal and the bottom of the cloth cable disk.

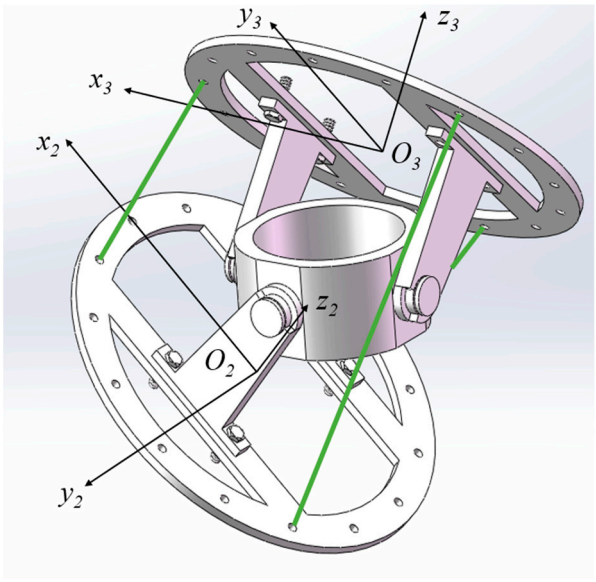


Figure 5. Cross universal joint model.

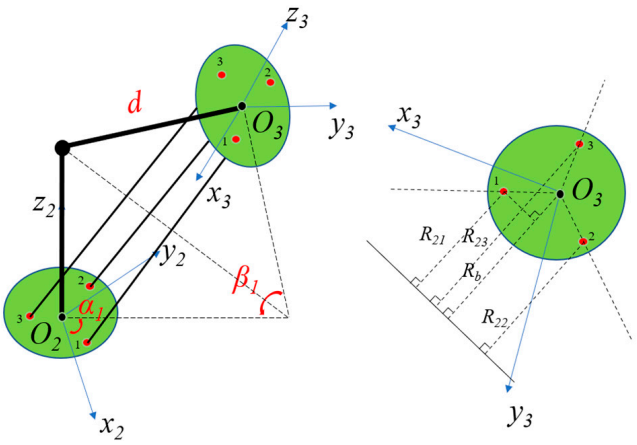


Figure 6. Cross universal joint structure sketch.

2.3.2. Mapping the Common Space to the Operational Space

Forward kinematic analysis.

From coordinate system $O_2 - X_2Y_2Z_2$ to coordinate system $O_3 - X_3Y_3Z_3$ can be viewed as coordinate system $O_2 - X_2Y_2Z_2$ rotated α_1 around the z axis, then rotated β_1 around the y axis, then translated s along the z axis, and finally rotated α_1 around the z axis to obtain coordinate system $O_3 - X_3Y_3Z_3$, the transformation matrix between coordinate systems can be expressed as:

$$
\begin{aligned}
{}^2_3T &= R_1 \cdot R_2 \cdot T_1 \cdot R_3 \\
&= \begin{bmatrix}
C^2\alpha_1C\beta_1 + S^2\alpha_1 & -C\alpha_1S\alpha_1 + C\alpha_1C\beta_1S\alpha_1 & C\alpha_1S\beta_1 & sC\alpha_1S\beta_1 \\
-C\alpha_1S\alpha_1 + C\alpha_1C\beta_1S\alpha_1 & C^2\alpha_1 + C\beta_1S^2\alpha_1 & S\alpha_1S\beta_1 & sS\alpha_1S\beta_1 \\
-C\alpha_1S\beta_1 & -S\alpha_1S\beta_1 & C\beta_1 & sC\beta_1 \\
0 & 0 & 0 & 1
\end{bmatrix}
\end{aligned}
\tag{16}
$$

where: $C\alpha_1 = cos\alpha_1, S\alpha_1 = sin\alpha_1, C\beta_1 = cos\beta_1, S\beta_1 = sin\beta_1, s = 2d \cdot \cos\frac{\beta_1}{2}$.

Inverse kinematic analysis.

In general, the defining equation for finding the spatial rotation angle of a mobile joint is:

$$p_x = s \cdot \cos\alpha_1 \sin\beta_1$$

$$p_y = s \cdot \sin\alpha_1 \sin\beta_1$$

$$p_z = s \cdot \cos\beta_1$$

$$\alpha_1 = \arctan\frac{p_y}{p_x} \tag{17}$$

$$\beta_1 = \arctan(\frac{p_y}{p_z \sin\alpha_1}) \tag{18}$$

2.3.3. Mapping Actuator Space to the Configuration Space

Inverse kinematic analysis.

As shown in Figure 6:

$$R_b = \frac{d}{\tan\frac{\beta_1}{2}}$$

$$R_{21} = R_b - r \cdot \cos(\alpha_1 - \frac{2\pi}{15})$$

$$R_{22} = R_b - r \cdot \cos(\frac{4\pi}{5} - \alpha_1)$$

$$R_{23} = R_b - r \cdot \cos(\frac{22\pi}{15} - \alpha_1)$$

$$l_{2,4} = 2R_{21}sin\frac{\beta_1}{2} = 2(\frac{d}{tan\frac{\beta_1}{2}} - r \cdot \cos(\alpha_1 - \frac{2\pi}{15}))sin\frac{\beta_1}{2} \tag{19}$$

$$l_{2,5} = 2R_{22}sin\frac{\beta_1}{2} = 2(\frac{d}{tan\frac{\beta_1}{2}} - r \cdot \cos(\frac{4\pi}{5} - \alpha_1))sin\frac{\beta_1}{2} \tag{20}$$

$$l_{2,6} = 2R_{23}sin\frac{\beta_1}{2} = 2(\frac{d}{tan\frac{\beta_1}{2}} - r \cdot \cos(\frac{22\pi}{15} - \alpha_1))sin\frac{\beta_1}{2} \tag{21}$$

where $l_{2,4}$, $l_{2,5}$, and $l_{2,6}$ are the lengths of cable 4, 5, and 6 in the second robotic arm, respectively.

Forward kinematic analysis.

From Equations (19)–(21):

$$\alpha_1 = \arctan\frac{\sqrt{3}(l_{2,5} - l_{2,6})}{2l_{2,4} - l_{2,5} - l_{2,6}} + \frac{2\pi}{15} \tag{22}$$

$$\begin{aligned}\beta_1 &= 2\arcsin\frac{l_{2,6} - l_{2,4}}{3r\cos(\alpha_1 - \frac{2\pi}{15}) - \sqrt{3}r\sin(\alpha_1 - \frac{2\pi}{15})} \\ &= 2\arcsin\frac{l_{2,5} - l_{2,4}}{3r\cos(\alpha_1 - \frac{2\pi}{15}) + \sqrt{3}r\sin(\alpha_1 - \frac{2\pi}{15})}\end{aligned} \tag{23}$$

2.4. Kinematic Modeling of Soft Robotic Arm

Based on the previous kinematic analysis and results of single-segment springs and movable joints, the kinematic simulation of the cable-driven soft robotic arm as a whole is performed.

2.4.1. Kinematic Modeling

The cable-driven soft robotic arm designed in this paper mainly consists of three soft continuums and two movable joints, and the kinematic analysis of the cable-driven soft robotic arm is now performed. The kinematic diagram is shown in Figure 7.

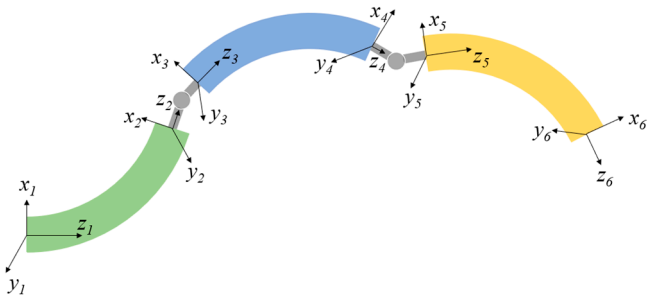


Figure 7. Structure diagram of soft manipulator.

2.4.2. Mapping the Configuration Space to the Task Space

Forward kinematic analysis.

The known variables for the forward kinematic analysis of the cable-operated soft robot arm are φ_i $\theta_i (i = 1, 2, 3)$ for the continuums of the spring body, and α_i and $\beta_i (i = 1, 2)$ for the movable joints, which leads to the solution of the pose of the end of the cable-operated soft robot arm in the working space.

Where ${}^{i-1}_{i}T$ $(i = 2, 3, 4, 5, 6)$ denotes the homogeneous transformation matrix from the coordinate system to $O_{i-1} - X_{i-1}Y_{i-1}Z_{i-1}$ the coordinate system $O_i - X_iY_iZ_i$. According to the homogeneous transformation matrix derived in the previous section and the "chain rule", the expression of the homogeneous transformation matrix ${}^{5}_{6}T$ can be obtained as:

$$ {}^{1}_{6}T = {}^{1}_{2}T \cdot {}^{2}_{3}T \cdot {}^{3}_{4}T \cdot {}^{4}_{5}T \cdot {}^{5}_{6}T $$

The expression for ${}^{i-1}_{i}T$ $(i = 2, 3, 4, 5, 6)$ is:

$$ {}^{i-1}_{i}T = \begin{bmatrix} C\theta_{\frac{i}{2}} C^2\varphi_{\frac{i}{2}} + S^2\varphi_{\frac{i}{2}} & -C\varphi_{\frac{i}{2}} S\varphi_{\frac{i}{2}} V\theta_{\frac{i}{2}} & C\varphi_{\frac{i}{2}} S\theta_{\frac{i}{2}} & \frac{C\varphi_{\frac{i}{2}} V\theta_{\frac{i}{2}}}{\rho} \\ -C\varphi_{\frac{i}{2}} S\varphi_{\frac{i}{2}} V\theta_{\frac{i}{2}} & C^2\varphi_{\frac{i}{2}} + C\theta_{\frac{i}{2}} S^2\varphi_{\frac{i}{2}} & S\varphi_{\frac{i}{2}} S\theta_{\frac{i}{2}} & \frac{S\varphi_{\frac{i}{2}} V\theta_{\frac{i}{2}}}{\rho} \\ -C\varphi_{\frac{i}{2}} S\theta_{\frac{i}{2}} & -S\varphi_{\frac{i}{2}} S\theta_{\frac{i}{2}} & C\theta_{\frac{i}{2}} & \frac{S\theta_{\frac{i}{2}}}{\rho} \\ 0 & 0 & 0 & 1 \end{bmatrix} (i = 2, 4, 6) \quad (24) $$

$$ {}^{i-1}_{i}T = \begin{bmatrix} C^2\alpha_1 C\beta_1 + S^2\alpha_1 & -C\alpha_1 S\alpha_1 + C\alpha_1 C\beta_1 S\alpha_1 & C\alpha_1 S\beta_1 & sC\alpha_1 S\beta_1 \\ -C\alpha_1 S\alpha_1 + C\alpha_1 C\beta_1 S\alpha_1 & C^2\alpha_1 + C\beta_1 S^2\alpha_1 & S\alpha_1 S\beta_1 & sS\alpha_1 S\beta_1 \\ -C\alpha_1 S\beta_1 & -S\alpha_1 S\beta_1 & C\beta_1 & sC\beta_1 \\ 0 & 0 & 0 & 1 \end{bmatrix} (i = 3, 5) \quad (25) $$

Inverse kinematic analysis.

The known variable for the inverse kinematics analysis of the cable-driven soft robotic arm is the end pose p_x, p_y, p_z, which is solved for the unknown variable $\varphi, \theta, \alpha, \beta$. According to the above, the formulas for solving the variables of each robotic arm can be obtained as follows:

$$ \varphi_{\frac{i}{2}} = \arctan\left(\frac{{}^{i-1}_{i}p_y}{{}^{i-1}_{i}p_x} \right), \quad (i = 2, 4, 6) \quad (26) $$

$$ \theta_{\frac{i}{2}} = 2\arctan \frac{{}^{i-1}_{i}p_y}{{}^{i-1}_{i}p_z \sin\varphi_1} (i = 2, 4, 6) \quad (27) $$

$$ \alpha_{\frac{i-1}{2}} = \arctan \frac{{}^{i-1}_{i}p_y}{{}^{i-1}_{i}p_x}, \quad (i = 3, 5) \quad (28) $$

$$\beta_{\frac{i-1}{2}} = \arctan\frac{{}^{i-1}_{i}p_y}{{}^{i-1}_{i}p_z \sin\alpha_1}, (i = 3, 5) \tag{29}$$

2.4.3. Mapping of Actuator Space to the Configuration Space

Inverse kinematic analysis.

The length of the cable $l_i (i = 1, 2, 3 \cdots 15)$ is:

$$l_1 = l_{1,1} = 2\sin\frac{\theta_1}{2}(\frac{l}{\theta_1} - r\cos\varphi)$$

$$l_2 = l_{1,2} = 2\sin\frac{\theta_1}{2}(\frac{l}{\theta_1} - r\cos(\frac{2\pi}{3} - \varphi_1))$$

$$l_3 = l_{1,3} = 2\sin\frac{\theta_1}{2}(\frac{l}{\theta_1} - r\cos(\frac{4\pi}{3} - \varphi_1))$$

$$l_4 = l_{1,4} + l_{2,4} = 2\sin\frac{\theta_1}{2}(\frac{l}{\theta_1} - r\cos(\varphi_1 - \frac{2\pi}{15})) + 2sin\frac{\beta_1}{2}(\frac{d}{tan\frac{\beta_1}{2}} - r\cos(\alpha_1 - \frac{2\pi}{15}))$$

$$l_5 = l_{1,5} + l_{2,5} = 2\sin\frac{\theta_1}{2}(\frac{l}{\theta_1} - r\cos(\frac{4\pi}{5} - \varphi_1)) + 2sin\frac{\beta_1}{2}(\frac{d}{tan\frac{\beta_1}{2}} - r\cos(\frac{4\pi}{5} - \alpha_1))$$

$$l_6 = l_{1,6} + l_{2,6} = 2\sin\frac{\theta_1}{2}(\frac{l}{\theta_1} - r\cos(\frac{22\pi}{15} - \varphi_1)) + 2sin\frac{\beta_1}{2}(\frac{d}{tan\frac{\beta_1}{2}} - r\cos(\frac{22\pi}{15} - \alpha_1))$$

$$l_7 = l_{1,7} + l_{2,7} + l_{3,7} = 2\sin\frac{\theta_1}{2}(\frac{l}{\theta_1} - r\cos(\varphi_1 - \frac{4\pi}{15})) + 2sin\frac{\beta_1}{2}(\frac{d}{tan\frac{\beta_1}{2}} - r\cos(\alpha_1 - \frac{4\pi}{15}))$$
$$+2\sin\frac{\theta_2}{2}(\frac{l}{\theta_2} - r\cos(\varphi_2 - \frac{4\pi}{15}))$$

$$l_8 = l_{1,8} + l_{2,8} + l_{3,8} = 2\sin\frac{\theta_1}{2}(\frac{l}{\theta_1} - r\cos(\frac{14\pi}{15} - \varphi_1)) + 2sin\frac{\beta_1}{2}(\frac{d}{tan\frac{\beta_1}{2}} - r\cos(\frac{14\pi}{15} - \alpha_1))$$
$$+2\sin\frac{\theta_2}{2}(\frac{l}{\theta_2} - r\cos(\frac{14\pi}{15} - \varphi_2))$$

$$l_9 = l_{1,9} + l_{2,9} + l_{3,9} = 2\sin\frac{\theta_1}{2}(\frac{l}{\theta_1} - r\cos(\frac{8\pi}{5} - \varphi_1)) + 2sin\frac{\beta_1}{2}(\frac{d}{tan\frac{\beta_1}{2}} - r\cos(\frac{8\pi}{5} - \alpha_1))$$
$$+2\sin\frac{\theta_2}{2}(\frac{l}{\theta_2} - r\cos(\frac{8\pi}{5} - \varphi_2))$$

$$l_{10} = l_{1,10} + l_{2,10} + l_{3,10} + l_{4,10} = 2\sin\frac{\theta_1}{2}(\frac{l}{\theta_1} - r\cos(\varphi_1 - \frac{2\pi}{5})) + 2\sin\frac{\beta_1}{2}(\frac{d}{\tan\frac{\beta_1}{2}} - r\cos(\alpha_1 - \frac{2\pi}{5}))$$
$$+2\sin\frac{\theta_2}{2}(\frac{l}{\theta_2} - r\cos(\varphi_2 - \frac{2\pi}{5})) + 2\sin\frac{\beta_2}{2}(\frac{d}{\tan\frac{\beta_2}{2}} - r\cos(\alpha_2 - \frac{2\pi}{5}))$$

$$l_{11} = l_{1,11} + l_{2,11} + l_{3,11} + l_{4,11} = 2\sin\frac{\theta_1}{2}(\frac{l}{\theta_1} - r\cos(\frac{16\pi}{15} - \varphi_1)) + 2\sin\frac{\beta_1}{2}(\frac{d}{\tan\frac{\beta_1}{2}} - r\cos(\frac{16\pi}{15} - \alpha_1))$$
$$+2\sin\frac{\theta_2}{2}(\frac{l}{\theta_2} - r\cos(\frac{16\pi}{15} - \varphi_2)) + 2\sin\frac{\beta_2}{2}(\frac{d}{\tan\frac{\beta_2}{2}} - r\cos(\frac{16\pi}{15} - \alpha_2))$$

$$l_{12} = l_{1,12} + l_{2,12} + l_{3,12} + l_{4,12} = 2\sin\frac{\theta_1}{2}(\frac{l}{\theta_1} - r\cos(\frac{26\pi}{15} - \varphi_1)) + 2\sin\frac{\beta_1}{2}(\frac{d}{\tan\frac{\beta_1}{2}} - r\cos(\frac{26\pi}{15} - \alpha_1))$$
$$+2\sin\frac{\theta_2}{2}(\frac{l}{\theta_2} - r\cos(\frac{26\pi}{15} - \varphi_2)) + 2\sin\frac{\beta_2}{2}(\frac{d}{\tan\frac{\beta_2}{2}} - r\cos(\frac{26\pi}{15} - \alpha_2))$$

$$l_{13} = l_{1,13} + l_{2,13} + l_{3,13} + l_{4,13} + l_{5,13} = 2\sin\frac{\theta_1}{2}\left(\frac{l}{\theta_1} - r\cos\left(\varphi_1 - \frac{8\pi}{15}\right)\right) + 2\sin\frac{\beta_1}{2}\left(\frac{d}{\tan\frac{\beta_1}{2}} - r\cos\left(\alpha_1 - \frac{8\pi}{15}\right)\right)$$
$$+2\sin\frac{\theta_2}{2}\left(\frac{l}{\theta_2} - r\cos\left(\varphi_2 - \frac{8\pi}{15}\right)\right) + 2\sin\frac{\beta_2}{2}\left(\frac{d}{\tan\frac{\beta_2}{2}} - r\cos\left(\alpha_2 - \frac{8\pi}{15}\right)\right)$$
$$+2\sin\frac{\theta_3}{2}\left(\frac{l}{\theta_3} - r\cos\left(\varphi_3 - \frac{8\pi}{15}\right)\right)$$

$$l_{14} = l_{1,14} + l_{2,14} + l_{3,14} + l_{4,14} + l_{5,14} = 2\sin\frac{\theta_1}{2}\left(\frac{l}{\theta_1} - r\cos\left(\frac{6\pi}{5} - \varphi_1\right)\right) + 2\sin\frac{\beta_1}{2}\left(\frac{d}{\tan\frac{\beta_1}{2}} - r\cos\left(\frac{6\pi}{5} - \alpha_1\right)\right)$$
$$+2\sin\frac{\theta_2}{2}\left(\frac{l}{\theta_2} - r\cos\left(\frac{6\pi}{5} - \varphi_2\right)\right) + 2\sin\frac{\beta_2}{2}\left(\frac{d}{\tan\frac{\beta_2}{2}} - r\cos\left(\frac{6\pi}{5} - \alpha_2\right)\right)$$
$$+2\sin\frac{\theta_3}{2}\left(\frac{l}{\theta_3} - r\cos\left(\frac{6\pi}{5} - \varphi_3\right)\right)$$

$$l_{15} = l_{1,15} + l_{2,15} + l_{3,15} + l_{4,15} + l_{5,15} = 2\sin\frac{\theta_1}{2}\left(\frac{l}{\theta_1} - r\cos\left(\frac{28\pi}{15} - \varphi_1\right)\right) + 2\sin\frac{\beta_1}{2}\left(\frac{d}{\tan\frac{\beta_1}{2}} - r\cos\left(\frac{28\pi}{15} - \alpha_1\right)\right)$$
$$+2\sin\frac{\theta_2}{2}\left(\frac{l}{\theta_2} - r\cos\left(\frac{28\pi}{15} - \varphi_2\right)\right) + 2\sin\frac{\beta_2}{2}\left(\frac{d}{\tan\frac{\beta_2}{2}} - r\cos\left(\frac{28\pi}{15} - \alpha_2\right)\right)$$
$$+2\sin\frac{\theta_3}{2}\left(\frac{l}{\theta_3} - r\cos\left(\frac{28\pi}{15} - \varphi_3\right)\right)$$

where $l_{i,k}$ represents the length of cable k in the mechanical arm of section i, and l_j is the length of cable j in the entire robotic arm.

3. Simulation and Results Analysis

3.1. Motion Space Simulation

3.1.1. Monte Carlo Method

The robot workspace is defined as the set of poses that can be reached from an end-effector reference point in the base coordinate system. The workspace solution methods mainly include geometric, analytical, and numerical methods. The geometric method is simple and intuitive, but as the number of degrees of freedom increases, the geometric shapes become very complex and difficult to understand, and it is difficult to express the motion of the robot in three-dimensional space. The analytical method generally adopts the theory of differential geometry to describe and calculate various singular surfaces according to the relationship between the workspace boundary and the singularity of the Jacobi matrix of the robot speed, and then uses the ingestion method and optimization theory to determine whether the singular surface is the boundary of the workspace, and finally calculates the boundary surface. Such a solution process is very complicated and generally not generalized. The Monte Carlo method is a simple, practical, and almost generalized numerical method, which has been widely adopted with the development of computer technology.

3.1.2. Movement Space of Soft Robot Arm

As shown in Figure 8, a is the motion space of a single soft body, b is the motion space of a cross universal joint, and c is the motion space of the entire soft mechanical arm. The length of the spring l is set to 180 mm, the maximum bending angle is 45 degrees, the total length of the cross universal joint is 54 mm, and the maximum allowable bending angle is 30 degrees. Within the maximum allowable bending angle, there is no interference between the rope and the robotic arm.

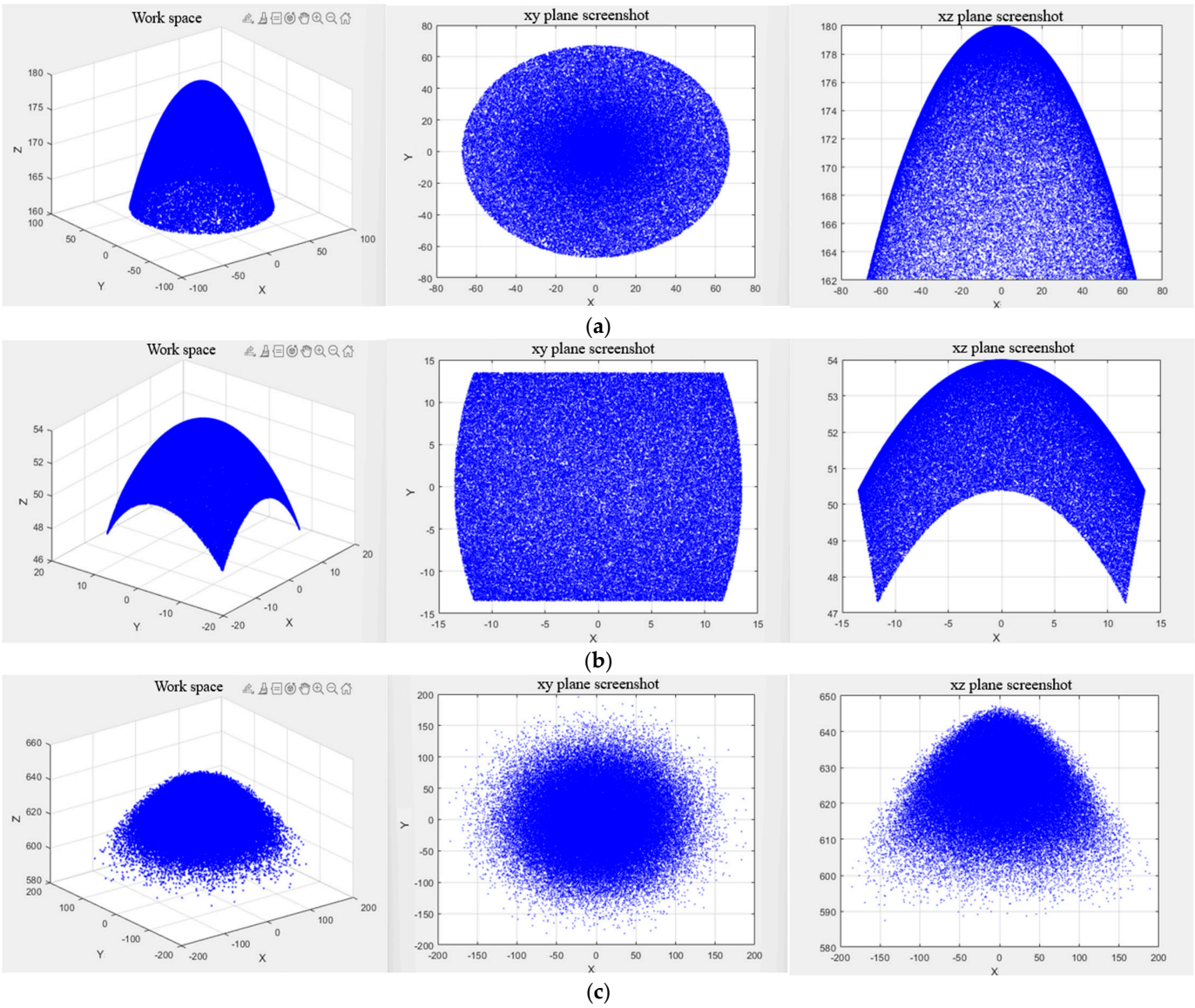


Figure 8. Motion space. (**a**) Single-stage soft body. (**b**) Cross gimbal. (**c**) The entire robotic arm.

3.2. Simulation Verification and Analysis

The simplified model of the single-segment soft body is set up and simulated by ADAMS, the simulation time is set to 12 s, and one cycle of reciprocating motion is performed in 12 s. The simplified model of the single-segment soft body is shown in Figure 9. The simulation results are shown in Figure 10 for the simulation results of the end pose, Figure 11 for the simulation results of the length of cable 1, Figure 12 for the simulation results of cable 2, and Figure 13 for the simulation results of cable 3.

When t = 2 s:

$$l_{1,1} = 172.3248$$

$$l_{1,2} = 172.2863$$

$$l_{1,3} = 185.9078$$

From Equations (14) and (15):

$$\varphi_1 = \arctan\frac{\sqrt{3}(l_{1,2} - l_{1,3})}{2l_{1,1} - l_{1,2} - l_{1,3}} = 60.14^\circ$$

$$\theta_1 = 2arcsin\frac{l_{1,3} - l_{1,1}}{r\left(3\cos\varphi_1 + \sqrt{3}\sin\varphi_1\right)} = 11.62^\circ$$

From Equations (3)–(5):

$$p_x = \frac{cos\varphi_1(1 - cos\theta_1)}{\rho} = 9.0612$$

$$p_y = \frac{sin\varphi_1(1 - \cos\theta_1)}{\rho} = 15.7936$$

$$p_z = \frac{sin\theta_1}{\rho} = -178.8781$$

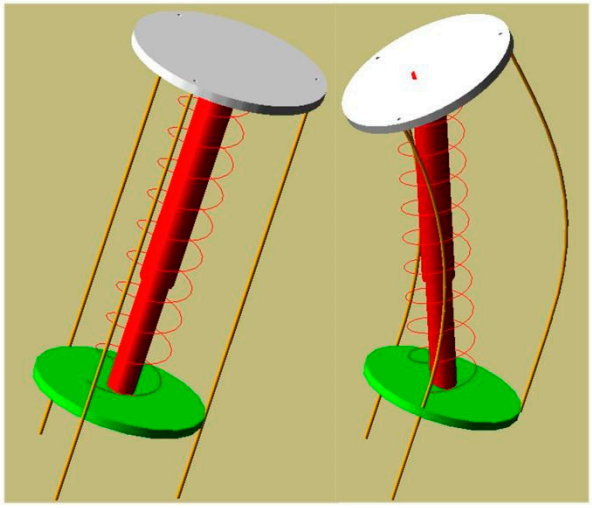


Figure 9. Simplified model of a single-segment soft body.

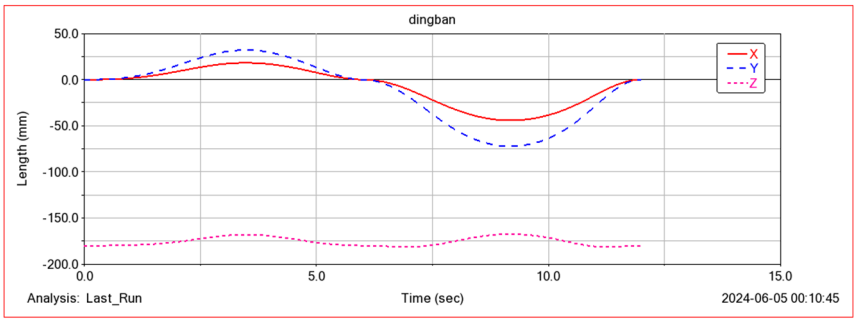


Figure 10. End pose.

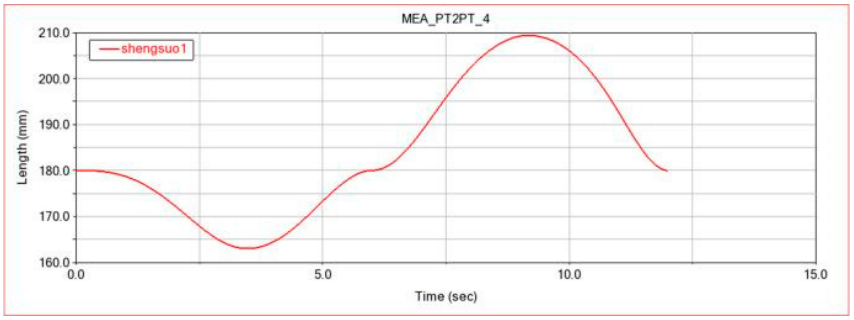


Figure 11. Length of cable 1.

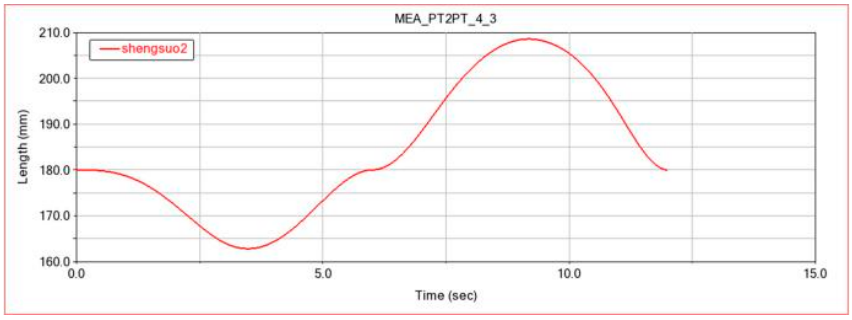


Figure 12. Length of cable 2.

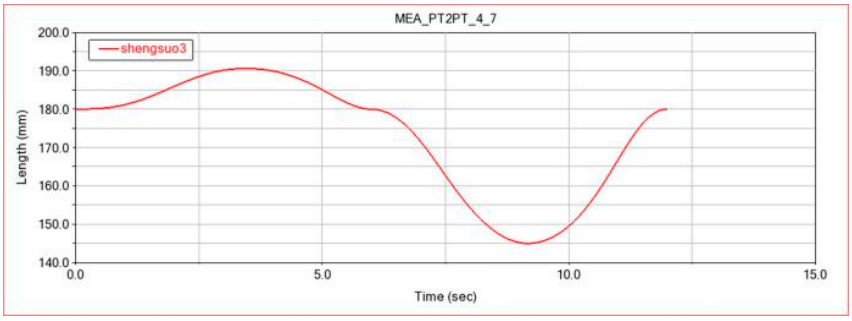


Figure 13. Length of cable 3.

The length of the cable can be obtained from the simulation data, the rotation angle and bending angle can be obtained from the relationship between the cable length and the joint angle, and then the theoretical value of the end pose can be calculated. As shown in Table 1, the numerical values of the theoretical coordinates and the actual coordinates when t = 2 s. Through the comparison of the two groups of data, the error is about 2%, which is within the reasonable error range. The length of rope l is 180 mm.

Table 1. Theoretical and actual values of end pose.

	Theoretical Value	Simulation Value
X	9.06	8.81
Y	15.79	15.40
Z	−178.88	−176.00

When t = 9 s:

$$p_x = -44$$

$$p_y = -71.9$$

$$p_z = -168$$

From Equations (6) and (7):

$$\varphi_1 = 238.54^\circ$$

$$\theta_1 = 53.28^\circ$$

From Equations (11)–(13):

$$l_{1,1} = 193.71$$

$$l_{1,2} = 192.36$$

$$l_{1,3} = 132.74$$

The end pose can be obtained from the simulation data, the joint angle is obtained from the relationship between the end pose and the joint angle, and then the theoretical

value of the cable length is calculated. As shown in Table 2, the numerical values of the theoretical length and the actual length when t = 9 s. By comparing the two sets of data, the error is about 8%.

Table 2. Theoretical and actual values of cable lengths.

	Theoretical Value	Simulation Value
$l_{1,1}$	193.71	209.20
$l_{1,2}$	192.36	208.41
$l_{1,3}$	132.74	145.16

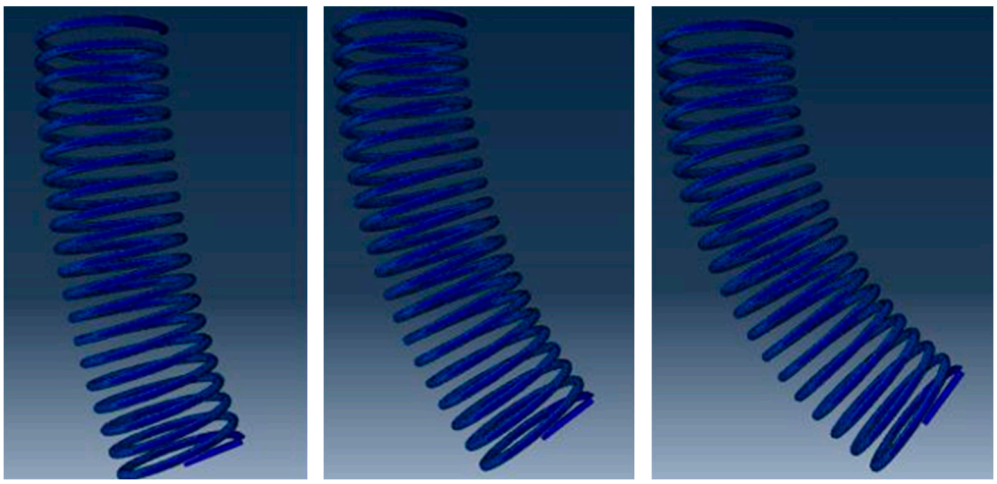
3.3. Performance Test and Analysis of Single-Segment Soft Body

Three cables were used to drive the soft body. When only one of the cables was used to drive the soft body, the soft body was made of spring steel material, and the relationship between the degree of bending of the soft body and the magnitude of the driving force of the cables was analyzed, as shown in Table 3 for the correspondence between the pose of the end of the soft body and the driving force.

Table 3. Driving force and pose of the simulation model.

Driving Force (N)	X	Z
0	0	180.00
5	31.10	177.35
9	57.56	167.17
15	78.73	153.51

As shown in the Figure 14, when the driving force is 0 N, the bending angle is minimized to 0 degrees; when the driving force is gradually increased to 15 N, the bending angle is gradually increased to about 54 degrees.



(**a**) (**b**) (**c**)

Figure 14. Experimental diagram of bending simulation. (**a**) When the force T = 5 N. (**b**) When the force T = 9 N. (**c**) When the force T = 15 N.

For the physical model, the experimental setup shown in Figure 15 was built under the condition of a single cable drive for the bending test, and the bending results were calibrated and sampled by using grid paper to obtain the bending degree of the soft body under different driving forces.

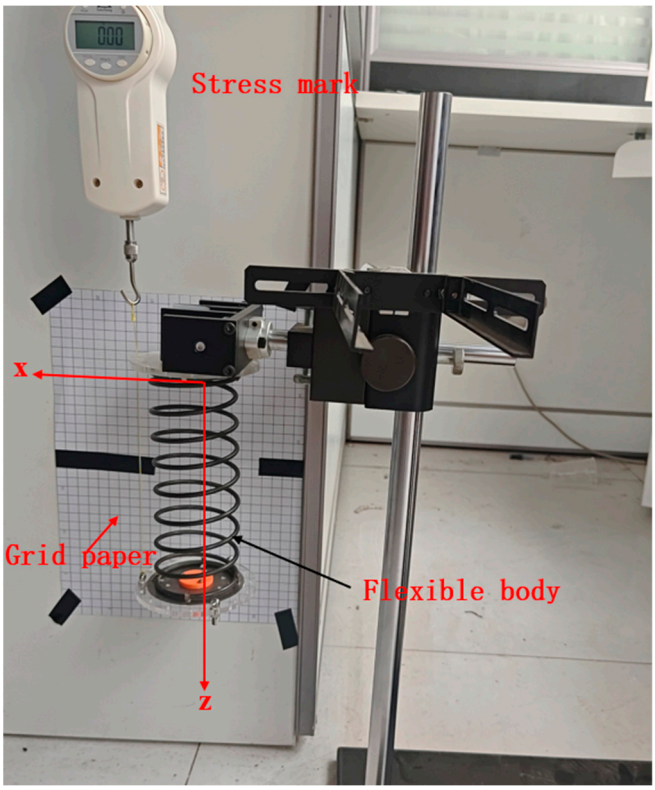


Figure 15. Experimental platforms.

The final pose of the soft body during bending is shown in Table 4.

Table 4. Physical model drivers as a function of location.

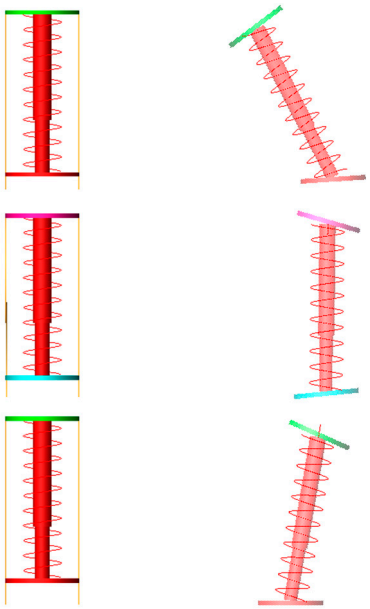
Driving Force (N)	X	Z
0	0	180.00
5	35.5	171.50
9	68.5	159.50
15	91.0	143.50

Due to the existence of handmade products in the production process, there will be a certain deviation of the soft body in force bending, which is mainly due to the existence of axial compression of the soft body in bending, and the processing of parts will be caused by the error.

3.4. Performance Test and Analysis of Three-Stage Soft Body

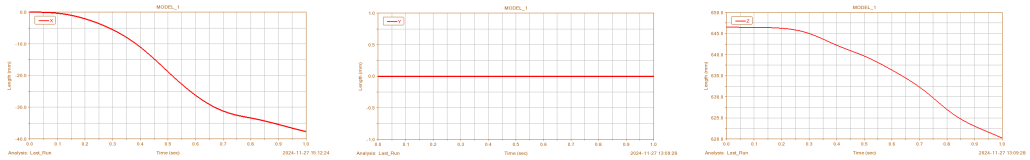
In order to be able to reduce the complexity of modeling and simulation, it is assumed that the robotic arm moves only in the xz plane. The spring section is pulled by cables, the cross universal joint is replaced by a revolute joint, the center of rotation is in the middle of the two spring sections, the axis of rotation is perpendicular to the xz plane, and the angle of rotation is set to 30 degrees.

As shown in Figure 16, a represents the posture of the robotic arm when it is not moving, and b shows the posture after the movement has been completed. As illustrated in Figure 17, a depicts the change in the x-coordinate, b shows the change in the y-coordinate, and c illustrates the change in the z-coordinate. In Figure 18, a represents the change in the length of cable 1, b shows the change in the length of cable 2, and c illustrates the change in the length of cable 3.



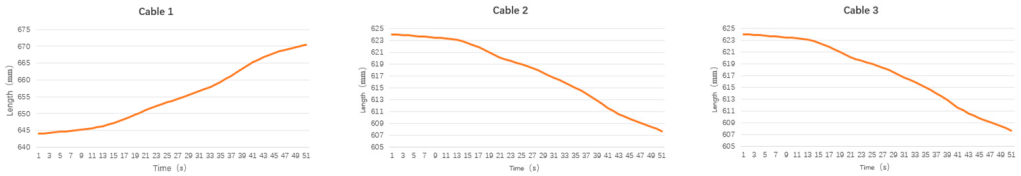
(**a**) (**b**)

Figure 16. Comparison of poses before and after simulation. (**a**) Posture in the natural state. (**b**) Posture after movement.



(**a**) (**b**) (**c**)

Figure 17. Change in the end-effector coordinates of the robotic arm. (**a**) x-coordinate. (**b**) y-coordinate. (**c**) z-coordinate.

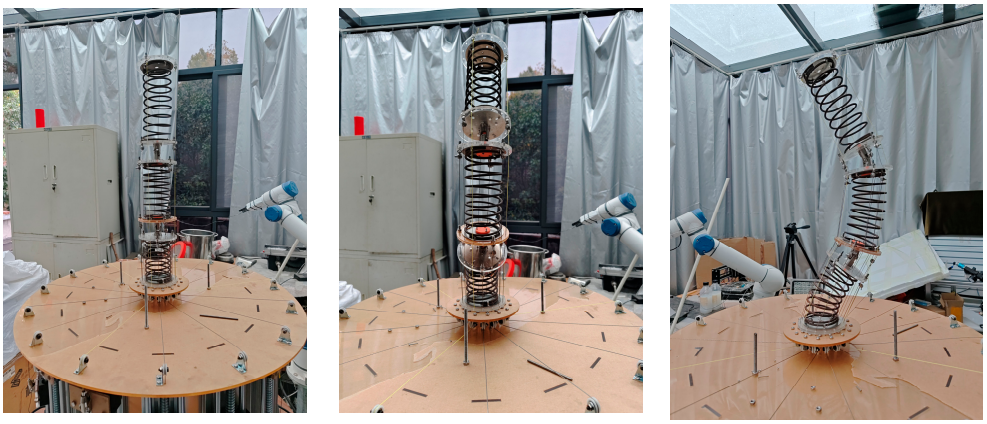


(**a**) (**b**) (**c**)

Figure 18. Change in rope length. (**a**) Length of Cable 1. (**b**) Length of Cable 2. (**c**) Length of Cable 3.

In order to objectively describe the operation of the soft robot arm, experiments and observations were carried out on the soft robot arm at the initial position (not working) and the fixed position (working). In the control system, 15 stepper motors were simultaneously driven to rotate the corresponding changing angles. The experimental results are shown in Figure 19, where a is the initial position, b is the front view, and c is the side view.

From the experiments, it can be seen that the motion state of the soft mechanical arm basically meets the requirements of the experimental theory when it rotates through the rigid joint axis, thus further verifying the correctness of the kinematic model.



(**a**) (**b**) (**c**)

Figure 19. Comparison of results before and after the experiment. (**a**) Posture of the robotic arm in natural state. (**b**) Posture after movement (front view). (**c**) Posture after movement (side view).

4. Conclusions

In this paper, a cable-driven soft robotic arm combining a soft body and a cross gimbal is designed, which can significantly increase the movement space of the cable compared with the traditional cable-driven soft robotic arm. Based on the segmented constant curvature method and the D–H method, respectively, the kinematics of a single-segment soft body, a cross gimbal, and a soft robotic arm as a whole are solved, and the mapping between the actuator space and the configuration space and between the configuration space and the task space is constructed and solved. The motion space of single-segment soft body, cross gimbal, and soft robotic arm as a whole in three-dimensional space is derived by MATLAB, and the simulation analysis of a single-segment soft body is carried out using ADAMS to find out the actual values of the end pose and cable length at different time points, and compare them with the theoretical values obtained by kinematic solution. The error is only 2~8%, which is within the permissible range, indicating that the proposed cable-driven soft body has a very good performance. It shows that the proposed kinematic model of the cable-driven soft robotic arm is effective and can be used to control the motion of the soft robotic arm.

Author Contributions: Conceptualization, F.W. and K.L.; methodology, F.W. and K.L.; software, K.L.; validation, F.W. and K.L.; formal analysis, Y.Z.; investigation, K.L.; resources, J.J.; data curation, Y.Z.; writing—original draft preparation, K.L.; writing—review and editing, K.L.; visualization, J.J.; supervision, F.W.; project administration, Y.Z. and J.J.; funding acquisition, F.W. All authors have read and agreed to the published version of the manuscript.

Funding: This research was funded by the Doctoral Fund of Henan Polytechnic University (Grant No. B2019-50), the Outstanding Young Scientists in Beijing (Grant No. BJJWZYJH01201910006021), the Open Foundation of the State Key Laboratory of Fluid Power and Mechatronic Systems (Grant No. GZKF-202016), the Henan Province Science and Technology Key Project (Grant Nos. 202102210081, 212102210050), the Key Research Projects of Higher Education Institutions in Henan Province (Grant No. 24A460014), the 2023 National Postdoctoral Researcher Funding Program (Grant No. GZC20230703), and the Science and Technology Assault on Problems in Henan Province for 2024 (Grant No. 242102221050).

Data Availability Statement: Data are contained within the article.

Conflicts of Interest: The authors declare no conflicts of interest.

References

1. Webster, R.J., III; Jones, B.A. Design and kinematic modeling of constant curvature continuum robots: A review. *Int. J. Robot. Res.* **2010**, *29*, 1661–1683. [CrossRef]
2. Li, C.; Rahn, C.D. Design of continuous backbone, cable-driven robots. *J. Mech. Des.* **2002**, *124*, 265–271. [CrossRef]

3. Walker, I.D. Continuous backbone "continuum" robot manipulators. *ISRN Robot.* **2013**, *2013*, 726506. [CrossRef]
4. Frazelle, C.G.; Kapadia, A.D.; Fry, K.E.; Walker, I.D. Teleoperation mappings from rigid link robots to their extensible continuum counterparts. In Proceedings of the 2016 IEEE International Conference on Robotics and Automation (ICRA), Stockholm, Sweden, 16–21 May 2016; pp. 4093–4100.
5. Pang, S.; Shang, W.; Zhang, F.; Zhang, B.; Cong, S. Design and stiffness analysis of a novel 7-DOF cable-driven manipulator. *IEEE Robot. Autom. Lett.* **2002**, *7*, 2811–2818. [CrossRef]
6. Renda, F.; Giorelli, M.; Calisti, M.; Cianchetti, M.; Laschi, C. Dynamic model of a multibending soft robot arm driven by cables. *IEEE Trans. Robot.* **2014**, *30*, 1109–1122. [CrossRef]
7. Cao, K.; Kang, R.; Branson, D.T., III; Geng, S.; Song, Z.; Dai, J.S. Workspace analysis of tendon-driven continuum robots based on mechanical interference identification. *J. Mech. Des.* **2017**, *139*, 062303. [CrossRef]
8. Runciman, M.; Avery, J.; Zhao, M.; Darzi, A.; Mylonas, G.P. Deployable, variable stiffness, cable driven robot for minimally invasive surgery. *Front. Robot. AI* **2020**, *6*, 141. [CrossRef] [PubMed]
9. Qi, F.; Ju, F.; Bai, D.; Wang, Y.; Chen, B. Kinematic analysis and navigation method of a cable-driven continuum robot used for minimally invasive surgery. *Int. J. Med. Robot. Comput. Assist. Surg.* **2019**, *15*, e2007. [CrossRef] [PubMed]
10. McMahan, W.; Chitrakaran, V.; Csencsits, M.; Dawson, D.; Walker, I.D.; Jones, B.A.; Pritts, M.; Dienno, D.; Grissom, M.; Rahn, C.D. Field trials and testing of the OctArm continuum manipulator. In Proceedings of the 2006 IEEE International Conference on Robotics and Automation, ICRA 2006, Orlando, FL, USA, 15–19 May 2006; pp. 2336–2341.
11. Calisti, M.; Giorelli, M.; Levy, G.; Mazzolai, B.; Hochner, B.; Laschi, C.; Dario, P. An octopus-bioinspired solution to movement and manipulation for soft robots. *Bioinspir. Biomim.* **2011**, *6*, 036002. [CrossRef] [PubMed]
12. Deimel, R.; Brock, O. A novel type of compliant and underactuated robotic hand for dexterous grasping. *Int. J. Robot. Res.* **2016**, *35*, 161–185. [CrossRef]
13. Gu, H.; Gao, H.; Zhao, Y.; Ma, X.; Wei, C. Dexterous obstacle-avoidance motion control of Rope Driven Snake Manipulator based on the bionic path following. *Mech. Mach. Theory* **2023**, *189*, 105406. [CrossRef]
14. Zheng, X.; Yang, T.; Zhu, X.; Chen, Z.; Wang, X.; Liang, B. Dynamic modeling and experimental verification of a cable-driven continuum manipulator with cable-constrained synchronous rotating mechanisms. *Nonlinear Dyn.* **2022**, *107*, 153–172. [CrossRef]
15. Li, X.; Xiong, Q.; Sui, D.; Zhang, Q.; Li, H.; Wang, Z.; Zheng, T.; Wang, H.; Zhao, J.; Zhu, Y. Disturbance-Adaptive Tapered Soft Manipulator with Precise Motion Controller for Enhanced Task Performance. *IEEE Trans. Robot.* **2024**, *40*, 3581–3601. [CrossRef]
16. Khalil, T.A.; Habib, S.; Seadby, S.G.; Maged, S.A. A structural optimization analysis of cable-driven soft manipulator. *Int. J. Adv. Robot. Syst.* **2024**, *21*, 17298806241246886. [CrossRef]
17. Cieślak, R.; Morecki, A. Elephant trunk type elastic manipulator—A tool for bulk and liquid materials transportation. *Robotica* **1999**, *17*, 11–16. [CrossRef]
18. Wang, H.; Zhang, R.; Chen, W.; Wang, X.; Pfeifer, R. A cable-driven soft robot surgical system for cardiothoracic endoscopic surgery: Preclinical tests in animals. *Surg. Endosc.* **2017**, *31*, 3152–3158. [CrossRef] [PubMed]
19. Zarebidoki, M.; Dhupia, J.S.; Liarokapis, M.; Xu, W. A cable-driven underwater robotic system for delicate manipulation of marine biology samples. *J. Field Robot.* **2024**, *41*, 2615–2629. [CrossRef]
20. Zhou, P.; Yao, J.; Zhang, S.; Wei, C.; Zhang, H.; Qi, S. A bioinspired fishbone continuum robot with rigid-flexible-soft coupling structure. *Bioinspiration Biomim.* **2022**, *17*, 066012. [CrossRef] [PubMed]
21. Zhang, J.; Li, Y.; Kan, Z.; Yuan, Q.; Rajabi, H.; Wu, Z.; Peng, H.; Wu, J. A preprogrammable continuum robot inspired by elephant trunk for dexterous manipulation. *Soft Robot.* **2023**, *10*, 636–646. [CrossRef] [PubMed]

Disclaimer/Publisher's Note: The statements, opinions and data contained in all publications are solely those of the individual author(s) and contributor(s) and not of MDPI and/or the editor(s). MDPI and/or the editor(s) disclaim responsibility for any injury to people or property resulting from any ideas, methods, instructions or products referred to in the content.